Soft Matter

Enhancement of Elastohydrodynamic Friction by Elastic Hysteresis in a Periodic Structure

Journal:	*Soft Matter*
Manuscript ID	SM-ART-10-2019-002087.R1
Article Type:	Paper
Date Submitted by the Author:	14-Dec-2019
Complete List of Authors:	Moyle, Nichole; Lehigh University Wu, Haibin; Cornell University, Department of Mechanical and Aerospace Engineering Khripin, Constantine; Michelin North America Inc Bremond, Florian; Michelin France Hui, Chung-Yuen; Cornell University, Theoretical and Applied Mechanics Jagota, Anand; Lehigh University, Bioengineering

Enhancement of Elastohydrodynamic Friction by Elastic Hysteresis in a Periodic Structure

Nichole Moyle[1], Haibin Wu[2], Constantine Khripin[3], Florian Bremond[4], Chung-Yuen Hui[2], Anand Jagota[1,5,*]

[1]Department of Chemical and Biomolecular Engineering, Lehigh University, Bethlehem, PA, USA
[2]Department of Mechanical and Aerospace Engineering, Cornell University, Ithaca, NY, USA
[3]Michelin North America Inc., Greenville, SC, USA
[4]Michelin Corporation, Clermont-Ferrand, France
[5]Department of Bioengineering, Lehigh University, Bethlehem, PA, USA.

*Communicating author: anj6@lehigh.edu

Abstract

Lubricated contacts are present in many engineering and biological systems involving soft solids. Typical mechanisms considered for controlling the sliding friction in such lubricated conditions involve bulk material compliance, fluid viscosity, viscoelastic response of the material (hysteretic friction), and breaking of the fluid film where dry contact occurs (adhesive friction). In this work we show that a two-phase periodic structure (TPPS), with a varying modulus across the sliding surface, provides significant enhancement of lubricated sliding friction when the system is in the elastohydrodynamic lubrication (EHL) regime. We propose that the enhanced friction is due to extra energy loss during periodic transitions of the sliding indenter between the compliant and stiff regions during which excess energy is dissipated through the fluid layer. This is a form of elastic hysteresis that provides a novel mechanism for friction enhancement in soft solids under lubricated conditions.

Introduction

The behavior of lubricated compliant contacts is important in many technological and natural settings such as between tires and a road surface, synovial joints, and contacting surfaces of animals that live in a wet environment. Increases in lubricated sliding friction for a multicomponent system, where compliance and viscosity are kept constant, is typically attributed to hysteretic or adhesive effects[1,2]. Increases in friction would not be expected in the elastohydrodynamic lubrication (EHL) regime where these effects are typically absent. Additionally friction is generally low in the EHL regime and thus methods to increase it are highly desirable in applications such as tires. Here we show that a surface patterned as a two phase periodic structure exhibits significant lubricated sliding friction enhancement over unstructured controls in the EHL regime, where by enhancement we mean increases in sliding friction. This is achieved through a new form of *elastic hysteresis,* in which energy is dissipated through the fluid rather than internally.

The behavior of lubricated contacts has been widely studied for elastic materials[3–5] traditionally with a focus on metal contacts which exhibit small deformations such as bearings[6,7] and pistons[8,9]. For more compliant materials the effect of deformations on the contact geometry and pressure profile, as well as hysteretic friction forces, becomes significant and must be considered[10–14]. One longstanding application for compliant lubricated contacts is the wet tire-road system, where both friction and wear have been studied[1,2,15–19]. Most of the work has focused on real tire systems which are multi-component materials and exhibit strong viscoelastic behavior. Other systems which could benefit from a better understanding of lubricated sliding mechanisms in compliant contacts include elastomeric seals[20], windshield wipers[21,22], and a number of biological systems such as synovial joints[23–25], contact lenses/eyelid wiping[24,26,27,] and skin contact[28–30].

The problem of liquid drainage for compliant contacts under lubricated conditions has been investigated for both thick and thin elastic layers[31–34]. A number of studies have examined lubricated sliding of compliant materials with a sphere-on-flat contact geometry to investigate the effects of properties such as material modulus, lubricant viscosity, bulk viscoelasticity, and surface roughness[35–42]. Other geometries have also been investigated experimentally, such as a ring on disc geometry to model the rubber/pipe interaction during deep water pipelaying and roll-shaped rubber sliding against a silica disk to model windshield wipers[21,43]. Models have been developed and compared to experimental work describing the effect of surface roughness as well as predicting sliding behavior in the mixed lubrication regime[10–12].

Studies have shown that contact geometry, material viscoelasticity, compliance (modulus), micro-hardness (for composite materials), surface roughness, lubricant viscosity, load and velocity all influence what lubrication regime a system is in, and also the friction response the material will exhibit in that regime. Typically, at high velocities and low loads the system is in the EHL regime, where there is a continuous fluid film between the two contacting surfaces. Material compliance and lubricant viscosity strongly affect the friction behavior in this regime. As velocity is decreased and load is increased, the system enters the mixed lubrication regime, where there are breaks in the fluid film. Here adhesive forces from the areas of dry contact as well as hysteretic forces from

material deformation begin to contribute to the friction response. In this regime sample roughness and viscoelasticity will typically affect the friction behavior. At low velocities and high loads the fluid may become completely excluded from the contact area and the system will enter the boundary lubrication regime, where the friction behavior is effectively that for the system in dry conditions[10].

Thus, despite the need to do so, there are few parameters available for modulating friction in the EHL regime. In this work we investigate whether this could be achieved by using surface structures to store and dissipate energy. Using structures as a mechanism to change the adhesion or friction behavior of an elastic *dry* contact has already been well established, often for materials which exhibit no bulk viscoelastic behavior. Biomimetic pillar/fibrillar structures have been widely studied for their enhancement of adhesion and static friction[44,45]. Ridge channel structures were shown to exhibit decreased sliding friction against smooth indenters and increased sliding friction against rough indenters[46]. Film terminated ridge channel structures were shown to provide sliding friction enhancements against smooth indenters and adhesion enhancements when rolling on a smooth surface[47,48]. These cases were all for non-lubricated conditions. Surface texturing has also been used widely to improve performance of lubricated contacts[49]. It promotes lift and hence reduces sliding friction by control of cavitation via texturing. It can also aid lubrication by surface dimples serving as lubricant reservoirs and traps for contaminant or debris particles. Our work differs in that it applies to a flat surface in which patterning takes the form of spatial variation of contact compliance.

Here, we report on friction (mostly in the EHL regime) of a two phase structure with periodic variation in elastic modulus. We find that one can significantly enhance friction of such a two phase periodic structured sample compared to unstructured controls composed of only the higher or the lower modulus material suggesting new mechanisms for friction enhancement. Two possible mechanisms for the lubricated sliding friction enhancement were considered, one due to shear deformation of the material in the sliding direction and the second due to energy loss through the fluid as the indenter transitions periodically from contact with one phase to the other.

Materials and Methods

1. Sample Fabrication

Samples were made from poly(dimethylsiloxane) (PDMS, Dow Sylgard 184, Dow Corning). The molding process for fabrication of TPPS (TPPS) samples is shown schematically in Figure 1.a (i-iv). A mold was machined out of aluminum with a ridge channel geometry, as is shown in Figure 1.a.i. Mold channel width, w_1, was 1.2mm, ridge width, w_2, was 0.8mm, and ridge height, d, was 1mm. The stiff portion of the structure was fabricated by casting a 10:1 base to cross linker mixture of PDMS into the mold as is shown in Figure 1.a.ii. The PDMS was cured on the mold at 80°C for 2 hours, then brought to room temperature and removed from the mold as shown in Figure 1.a.iii. Next a 30:1 base to cross linker mixture of PDMS was poured into the cured PDMS to form the soft portion of the structure as is shown in Figure 1.a.iv. The structure was cured again at 80° for 2 hours with a weighted glass slide on top of the 30:1 mixture, resulting

in only a thin layer of the 30:1 PDMS mixture covering the surface of the sample, making the entire surface chemically homogeneous. The final dimensions for the TPPS samples are labeled in Figure 1.a.iv (side view) and Figure 1.b (top view, under thin film layer) and are as follows; structure height, d, of 1mm, thin film thickness, t, of approximately 70 microns, total sample height, h, of 2 mm, stiff phase width, w_1, of 1.2mm, soft phase width, w_2, of 0.8mm, and structure period, w of 2mm. As the thin film was obtained using compression during curing, there is a small undulation of the surface in the direction normal to the stripes, with amplitudes less than 100 microns. The Young's modulus of the stiffer phase (10:1 base to cross linker ratio) is denoted by E_1 and is approximately 3MPa[50], while the Young's modulus of the softer phase (30:1 base to cross linker ratio) is denoted by E_2 and is approximately 190 kPa[51]. Two controls were fabricated to test friction properties of the two phases, and are shown schematically in Figure 1.c. The compliant control sample is shown in the bottom of Figure 1.c and is a 2mm thick slab of 30:1 base to cross linker mixture of PDMS, cured at 80°C for two hours. The stiff control sample is shown in the top of Figure 1.c, and was fabricated by first making a 2mm thick slab of 10:1 base to cross linker mixture of PDMS, cured at 80°C for two hours. Then, in a procedure similar to the TPPS fabrication, a layer of 30:1 base to cross linker PDMS mixture was poured onto the cured control sample and cured at 80°C for two hours while under a weighted slide, resulting in a thin layer of the softer material coating the top of the sample.

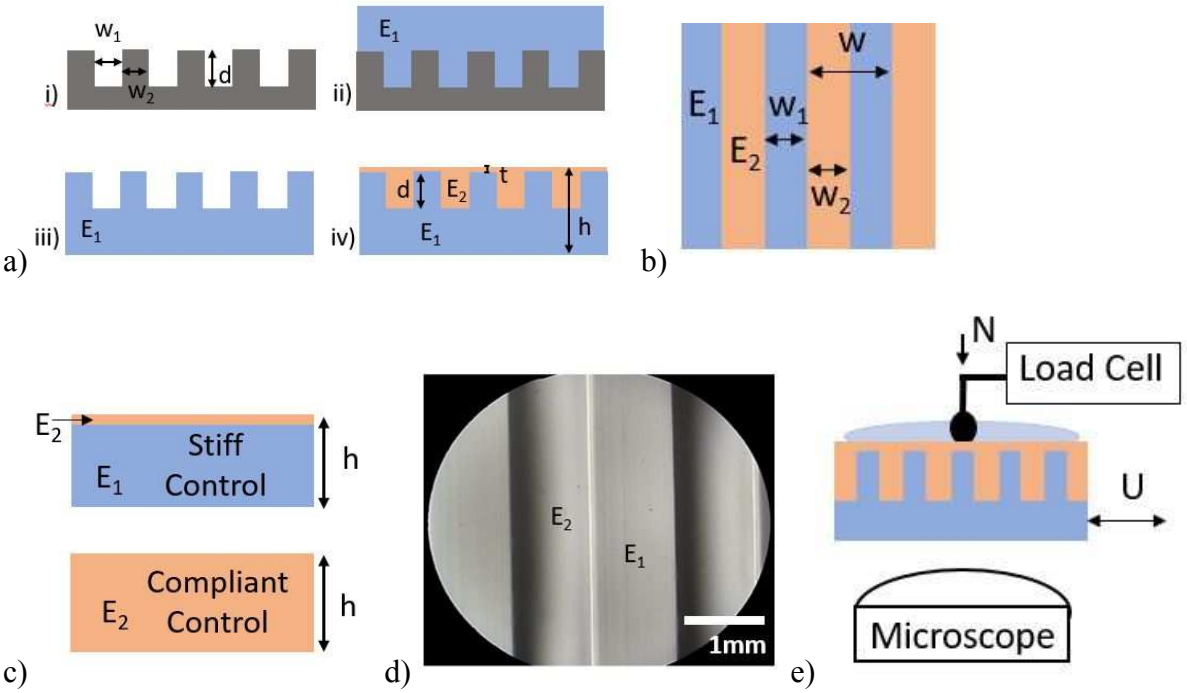

Figure 1. a) Schematic showing side view of molding procedure used for casting two phase periodic structure (TPPS). b) Schematic showing top view of two phase periodic structure (TPPS) under film layer. c) Schematics of control structures, top shows stiff control structure, bottom shows compliant control structure. d) Optical micrograph of TPPS e) Schematic of lubricated sliding experiment.

2. Lubricated Friction Experiments:

Sliding friction in a direction orthogonal to the stripes was measured under lubricated conditions. A schematic of the sliding experiment is shown in Figure 1.e. The surface of the sample was coated with a layer (approximately 1mm thick) of a highly wetting lubricant (PDMS base, viscosity η=5.1 Pa*s). A spherical glass indenter (R=0.5, 2mm, or 3mm) was brought into contact with the sample surface under a normal load ranging from 18.6 to 238.1mN and the sample was moved perpendicular to the applied load using a variable speed motor (Newport ESP MFA-CC) with velocities ranging from 0.025 to 1mm/s. The indenter was connected to a load cell (Honeywell Precision Miniature Load Cell) measuring the friction force resisting sample motion. Data was recorded for a full cycle of lubricated sliding, where a sample would be brought away from and then back to its starting position. Sample displacements for the controls were chosen based on how long it took for the force to reach steady state. For the two phase periodic structure sample a displacement of 10mm in each direction was always used in order to probe 5 full structure periods. To visualize motion during sliding, a small subgroup of experiments were performed with fluorescent particles mixed into the lubricant (Cospheric FMR-1.3, diameters of 1-5μm). Videos were analyzed using the particle tracking software TrackMate in the Fiji distribution of ImageJ.[52] All reported friction values are for clean lubricant with no particles to avoid their potential influence on measured friction. Experiments to assure that swelling from the lubricant was minimal for the length and time scales being probed during the experiment were performed, and showed no effect from swelling.

Results and Discussion

The two phase periodic structure (TPPS) studied in this work was composed of a commercial polydimethylsiloxane (PDMS) elastomer formulation with a flat surface patterned by stripes with alternating elastic moduli. Experiments tested the lubricated friction of the TPPS samples in a direction orthogonal to the stripes, and two control samples, a compliant control and a stiff control, with each control representing a portion of the TPPS structure. Friction was first measured against a 2mm radius spherical glass indenter for 72 different load and velocity combinations, with unreacted PDMS base used as the lubricant. Figure 2(a) shows typical data obtained for one cycle of the lubricated sliding experiments. It is evident that the measured friction behavior of the two flat controls is markedly different from that of the TPPS sample. As would be expected, both flat controls have a relatively constant friction force as the samples undergo cyclic lubricated sliding against the indenter. For the two phase periodic structure sample, however, frictional force varies periodically as the sample is moved relative to the indenter, with a maximal or minimal friction force every 2mm, the period of the sample surface structure.

An average friction force, f, can be calculated from the data in Figure 2(a) using the equation

$$f = \oint P du/\delta \qquad [1]$$

where P is the measured horizontal force, u is the sample displacement and δ is the total distance the sample travels during a cycle. (The integral on the RHS of eq. (1) is the energy loss in a cycle.) Applying equation (1) to an entire cycle could produce error as samples exhibited startup effects when changing direction. To avoid these effects, for the controls f was calculated only on portions of the curve on which force had reached steady state. For the structured sample, each cycle contained 5 periods (10 mm displacement in each direction) and equation (1) was applied to a 4mm section in the center of the cycle, sampling 2 complete periods. This avoided startup effects as well as any biasing of the data that could occur by measuring an incomplete period.

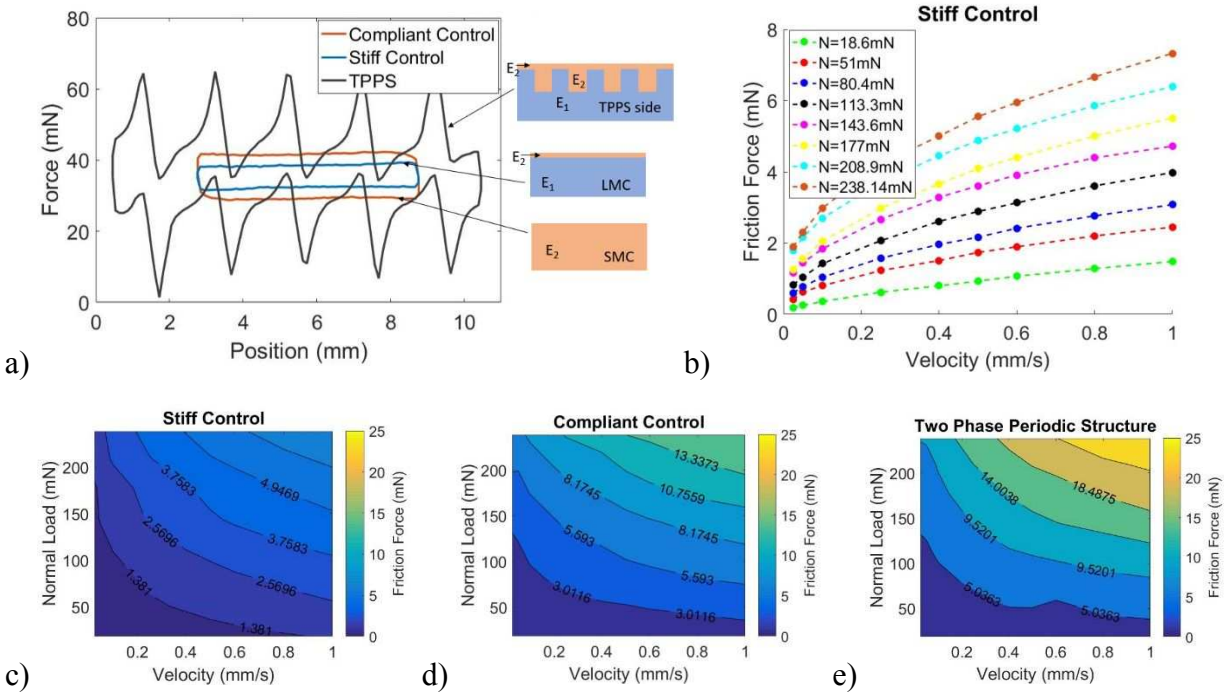

Figure 2. Lubricated sliding friction data for an indenter with radius R=2mm. a) Typical raw data for one cycle of the two phase periodic structure (TPPS) (black line), stiff control (blue line), and the compliant control (orange line) at a normal load of 113.3 mN and a velocity of 0.5 mm/s. b) Plot of friction force, f, for the stiff control for a range of velocity and load conditions. c-e) Contour plots of friction values for (c) stiff control (d) compliant control, and (e) TPPS in load-velocity space.

Figure 2(b) shows a plot containing friction forces of the stiff control for all load and velocity conditions tested. This plot shows that the largest friction values are obtained at the largest load and velocity conditions. The effect of velocity and load on the lubricated friction can also be visualized using a contour plot in load-velocity space. Figure 2(c) shows this plot for the data shown in Figure 2(b), while the equivalent data for the compliant control and the TPPS are shown as contour plots in Figure 2(d) and Figure 2(e), respectively. Comparing the three contour plots, it is clear that the velocity and load dependence of all three samples is similar for the parameter space tested. However, one striking difference between the three contour plots is the magnitude

of the friction forces measured. At high load and velocity conditions, the stiff control has friction is about 7 mN (Figure 2(c)) while for the compliant control it is about 15mN (Figure 2(d)). Because the TPPS presents chemically a uniform surface and mechanically a surface that is in nearly equal parts stiff control and complaint control, one might expect friction for TPPS to be bounded by that of the stiff control and the compliant control. However, contrary to this expectation, we measure friction for TPPS to be about 27mN for large velocity and normal load. That is, the TPPS sample has significantly higher friction at a given set of conditions than both controls.

To better quantify this increase in lubricated sliding friction exhibited by the TPPS a friction enhancement ratio, ε, was calculated. It is defined by

$$\varepsilon = \frac{f_{TPPS}}{0.4 * f_{Compliant} + 0.6 * f_{Stiff}}, \quad [2]$$

where $f_{,TPPS}$, $f_{Compliant}$, and f_{Stiff} are the friction values for the TPPS, compliant control, and stiff control respectively, and 0.4 and 0.6 represent the fraction of the surface area occupied by each phase. Table 1 shows enhancement ratios for velocities of 0.025, 0.5, and 1mm/s (additional data tables can be found in the SI). Inspection of Table 1 shows a friction enhancement ratio of 2 or higher for most of the conditions tested with the 2mm radius indenter, with a maximum value of 3.0 for a velocity of 0.025mm/s and a load of 80.4mN. Thus it is clear the TPPS provides significant lubricated friction enhancement (up to a factor of 3) over load and velocity ranges that span more than an order of magnitude for a spherical indenter with a diameter equal to the period of the structure.

Table 1. Friction enhancement ratios for the TPPS under lubricated sliding against 2mm and 0.5mm radius indenters. (See SI for definition of error)

Velocity								
	R=2mm						R=0.5mm	
	0.025 mm/s		0.5 mm/s		1 mm/s		0.5 mm/s	
load (mN)	ε	Error	ε	Error	ε	Error	ε	Error
18.6	1.9	0.1	1.75	0.05	1.69	0.04	1.7	0.3
51.0	2.76	0.05	2.3	0.1	2.1	0.1	1.4	0.1
80.4	3.0	0.2	2.32	0.04	2.15	0.02	1.24	0.05
113.3	2.9	0.1	2.37	0.02	2.30	0.02	1.19	0.03
143.6	2.7	0.1	2.48	0.01	2.6	0.1	1.09	0.02
177.0	2.6	0.1	2.55	0.04	2.51	0.02	0.95	0.01
208.9	2.2	0.1	2.49	0.03	2.47	0.03	1.0	0.2
238.1	2.2	0.1	2.48	0.02	2.55	0.02	1.20	0.02

To understand the mechanisms contributing to the observed friction enhancement of the TPPS it is critical to know in which lubrication regime the experiments are operating. Based on the magnitude of the sliding friction values, the compliance of the substrate, as well as the lack of dry contact observable during experiments it was hypothesized that experiments are in the EHL

regime (see SI for further discussion). To confirm this a scaling analysis was performed. As reviewed in detail in SI, isoviscous EHL theory shows that for a lubricated rigid sphere sliding steadily against the flat surface of an homogenous elastic substrate, the response depends on a single dimensionless parameter (a normalized velocity) given by

$$V = U\eta R^{5/3} G^{1/3} N^{-4/3} \quad [3]$$

where R is the sphere radius, G is the shear modulus of the substrate, N is the normal load, η is the (constant) viscosity of the lubricant, and U is the sliding velocity, as shown schematically in Figure 3(a). The value of G is well-defined for the stiff control and compliant control, whereas for the TPPS we used a value, G_{ave}, given by

$$G_{ave} = 0.4G_{Compliant} + 0.6G_{Stiff} \, . \quad [4]$$

which corresponds to the limit where the contact region is uniformly spread over a region much larger than the period of the structure. The normalized friction force F is found to be

$$F = fR^{2/3} G^{1/3} N^{-4/3} = F(V). \quad [5]$$

Figure 3(a) plots F versus V for lubricated sliding experiments (R=2mm indenter). The range of dimensionless velocity, V~10^{-4}-10^{-7}, in these experiments is similar to that for typical tire conditions (further details in SI). The blue circles in Figure 3(a) represent all data points plotted in Figure 2(b) (and the equivalent contour plot in Figure 2(c)) for the stiff control. Evidently, the EHL scaling collapses the 72 different velocity and load conditions tested with this control onto one master curve. The red circles in Figure 3(a) represent the same experimental conditions but for the compliant control, which were first plotted in Figure 2(d). Not only do the compliant control experiments also collapse onto one master curve when scaled, they do so onto the same master curve as the stiff control. This result strongly suggests that for these conditions the two controls are under lubricated sliding in the isoviscous EHL regime. Further validation that the controls are in the EHL regime is detailed in SI, utilizing a model for friction coefficient developed by Vicente et al.[35]. The green circles in Figure 3(a) represent data for the TPPS, Figure 2(e). These data also collapse onto a similar master curve albeit somewhat more scattered than for the controls. This likely comes from the fact that the steady-state EHL scaling is based on a homogeneous elastic-half space, and does not account for the periodic variation of substrate properties in the TPPS. Most significantly, the TPPS shows considerably higher normalized friction values than the controls at the same normalized velocities, again highlighting the friction enhancement of these structures.

A smaller subset of experiments using indenters with radii of 0.5mm and 3mm were tested in a similar load and velocity range as for previous experiments. When tested with a 3mm radius indenter the TPPS exhibited similar enhancements to those seen with the 2mm radius indenter (data tables in SI). The same is not true for experiments using the 0.5mm indenter, which for most load and velocities tested exhibited little or no enhancement for the TPPS; these results for an intermediate velocity of 0.5mm/s are listed in Table 1 (results for U=0.1 and U=1 mm/s in SI). Scaling of these additional data sets, plotted in Figure 3(b) along with the data for the 2mm radius

indenter, gives insight into why friction enhancement is lost with the decrease in indenter size. For the 3mm radius indenter, the controls and the TPPS results fall onto the same master curves as the data from the 2mm radius indenter experiments. In contrast, the scaled results for the 0.5mm indenter do not all fall on the same master curves as the larger indenter experiments. While the data for the stiff control collapse onto the same curve as the larger indenters, many of the results for the compliant control and the TPPS do not. For these latter samples, at low loads (large V) the data collapsed on the same master curves as the larger indenter experiments, but as load increased (small V) both diverged away from master curves towards larger normalized friction values. This divergence resulted in three separate curves each for the compliant control and the TPPS data, one for each velocity tested with the 0.5mm radius indenter (0.1, 0.5, and 1mm/s). This indicates that for the 0.5mm radius indenter we have probed conditions where the sliding contact is no longer operating in the EHL regime. Because departure from EHL occurs at low velocities and high loads, it is possible that the system is entering the mixed or boundary lubrication regime for the compliant control and TPPS samples. This departure from EHL lubrication resulted in and increase in friction but a loss of friction enhancement. For example at a load and velocity condition of 18.6mN and 0.5mm/s, which for the 0.5mm radius indenter has all three samples collapsing onto the curves of the larger indenters, a friction enhancement ratio of 1.7 was obtained, as listed in Table 1. For the same velocity and indenter diameter, increasing the load to 80.4 mN results in a divergence from the master curve obtained using larger indenters, and a reduced friction enhancement ratio of 1.2 was obtained.

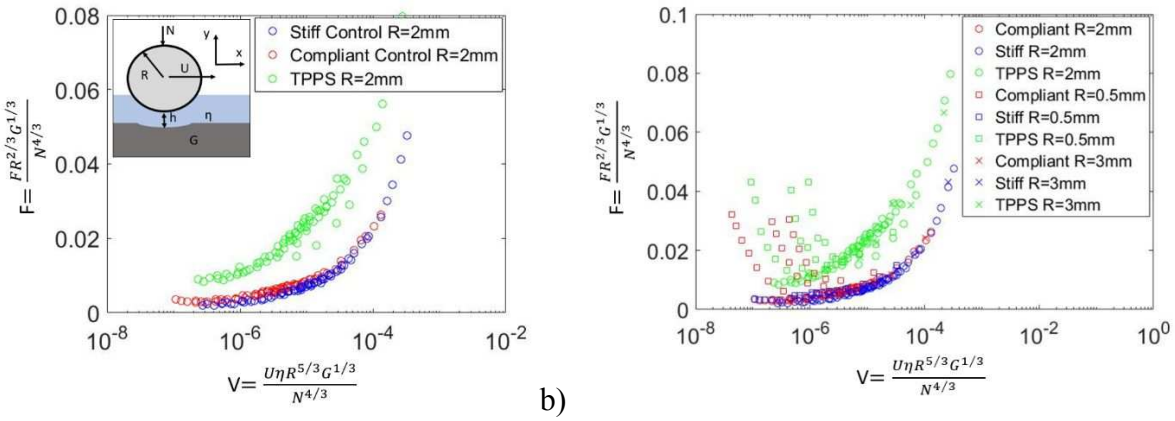

Figure 3. a) Plot of normalized friction force and normalized velocity for experiments with R=2mm indenter using EHL theory for scaling. b) Plot of normalized friction force and normalized velocity for experiments with R=0.5mm, R=2mm, and R=3mm indenters using EHL scaling.

When lubricated sliding friction enhancements are observed in composite materials the enhancements are often attributed to the composite providing additional dissipative contributions from viscoelastic effects in the material (hysteretic friction) and fluid film breakage where dry contact occurs (adhesive friction)[1,2,19]. However, in our case the data in Figure 3(a) collapse using purely isoviscous EHL scaling, so it is unlikely that these mechanisms are contributing to the observed friction enhancement. Thus it is unclear what the mechanisms for friction enhancement are; to gain further insight experiments were performed to visualize the fluid flow during sliding.

For this purpose we added fluorescent particles to the lubricant fluid. Dark field imaging studies focused on sliding against a 2mm radius indenter at an intermediate velocity of 0.5mm/s. Videos of the particle motion were recorded during sliding experiments, a typical still image from which is shown in Figure 4(a) for an experiment on a stiff control with a load of 18.6mN (Stiff_0p5mmps_18p6mN_FP_10x in SI). Even under the smallest load tested, the videos showed a region devoid of particles near the center of the contact. This indicates an area where the film thickness is less than the diameter of the particles (1-5 microns). That is, this region gives an indication of the effective contact area for a given set of conditions.

Videos were analyzed using particle tracking software (TrackMate[52]) to obtain streamlines. Figure 4(b) shows the particle tracking streamlines obtained by processing the video from which the still image of Figure 4(a) was taken. Particle tracking results were then used to calculate velocity vectors for each particle in each frame of the video, an example of which is shown in Figure 4(c) (full video vel_vect_Stiff_0p5mmps_18p6mN_10x in SI). As is evident from the video, there is considerable fluctuation in measured velocities, in part because the vertical position of each particle within the fluid is variable. For the cases where sliding occurs with steady state flow (in the frame of the indenter), such as for the stiff control, a time averaged velocity profile can be computed, as shown in Figure 4(d). Videos showing the particle velocity vectors during sliding as well as additional information on how the velocity vectors and averaged profiles were calculated are given in the SI.

Under a variety of load conditions, the velocity fields (in a frame of reference attached to the indenter) for both the stiff control and compliant control exhibited similar stable steady state flow. Qualitatively, the velocity fields are all similar with uniaxial flow far from the contact region, a radial component of the flow field (first outgoing and then incoming) near the "contact" region, and an inner "contact" region devoid of measurements from which marker particles are excluded. The size of this contact region increases with increasing normal load (additional videos and examples in SI), consistent with what would be expected due to the action of intervening fluid pressure.

The TPPS samples are not translationally invariant so their velocity fields did not exhibit steady state behavior. Figures 4(e)-(i) present still images from video (vel_vect_TPPS_0p5mmps_113p3mN_10x) detailing the instantaneous velocity field during sliding over one period of the structure. These still images are from an experiment with an intermediate normal load of 113.3mN. The yellow area represents the smaller modulus phase (soft), the area with no shading the larger modulus phase (stiff), and the black dot represents the lowest point of the indenter, i.e., roughly the center of the contact region. The flow behavior in Figures 4(e-i) have been matched to their respective locations on the force vs position plot in Figure 4(j) to aid in understanding the relationship between periodic features of the force response and the instantaneous flow field. At t_1=0s, Figure 4(e) shows a velocity profile similar to that in Figure 4(c) for the stiff control, as the center point of contact is near the center of the stiff phase. This corresponds to a plateau region on the curve in Figure 4(j), where the force is slowly decreasing. At t_2=1s in Figure 4(f), as the smaller modulus area of the structure approaches the center point of the indenter, particles approaching the indenter begin to move rapidly both in-line and

perpendicular to the sliding direction (i.e., approximately radially), with the radial flow becoming more severe at t_3=1.3s as shown in Figure 4(g). Figures 4 (f) and (g) correspond to a rapidly decreasing force to its minimum value, Figure 4 (j). The radial expulsion of particles eventually leads to a much larger contact region devoid of particles, as shown in Figure 4(h) at t_4=2s, indicating an increase in the effective contact region. This corresponds to an increasing force in Figure 4 (j). At t_5=3s, as the soft phase passes the center point of the indenter, this contact region rapidly decreases in size as particles flow inward, as shown in Figure 4(i). This corresponds to the point right after the force peak, where the force suddenly decreases rapidly in Figure 4 (j). At t=4s, the center point has traveled one period of the TPPS, and the position and flow behavior returns to what was shown in Figure 4(e); the cycle repeats. This observation of periodic unsteady velocity fields with accompanying changes in the contact region suggest the hypothesis that the sudden local transition in compliance provides a mechanism for unstable deformation and dissipation of energy, a new form of *Elastic Hysteresis*.

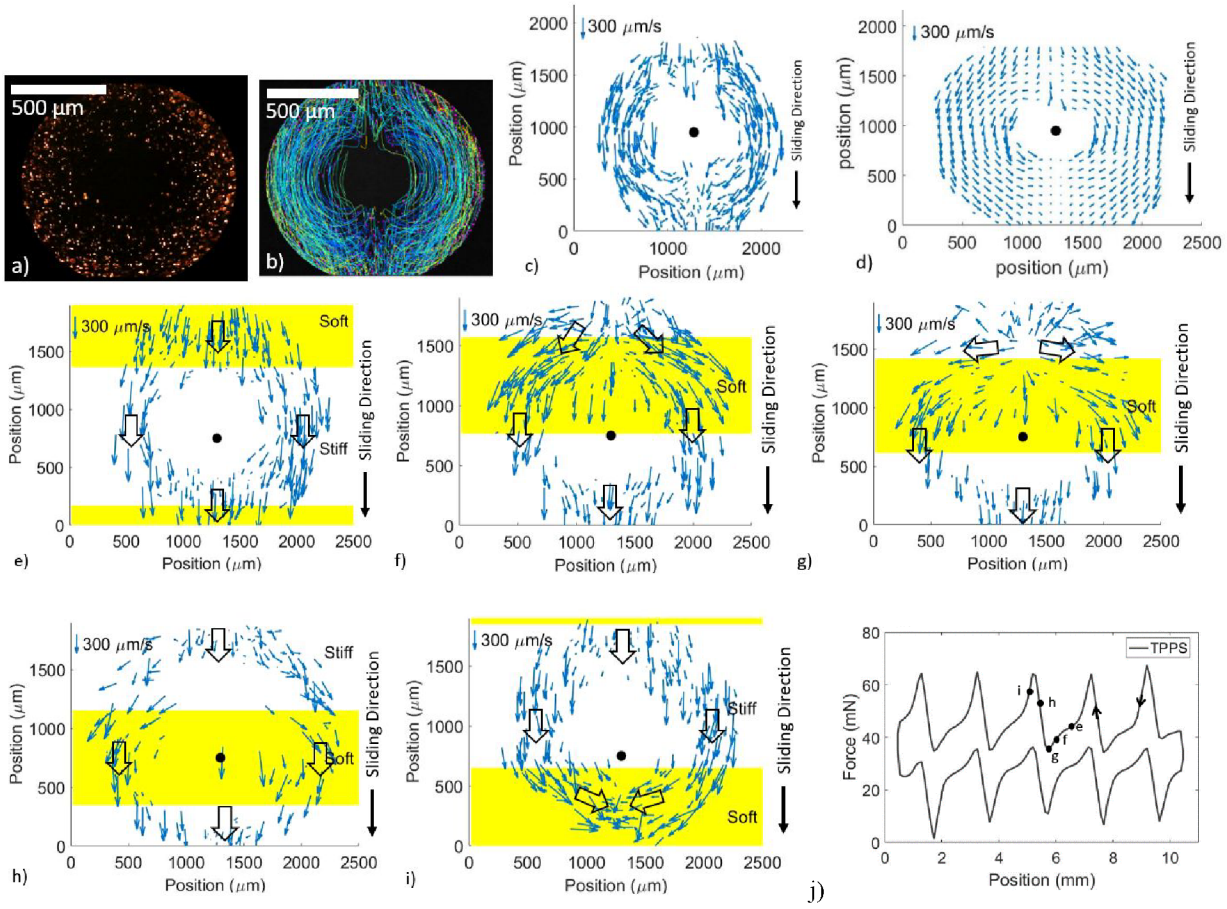

Figure 4. a-d) Particle tracking results and analysis for the stiff control with N=18.6mN and U=0.5mm/s. a) Frame from video. b) Streamlines from processed video. c) Frame from video of analyzed particle trajectories. d) Time-averaged velocity profile. e-i) Particle tracking results for TPPS with N=113.3mN and U= 0.5mm/s at times e) t1=0s f) t2=1s g) t3=1.3s h) t4=2s i) t5=3s. Black dots represent the lowest point of the indenter, sliding direction is of the sample relative to the indenter. j) Data from lubricated sliding experiments on the TPPS sample under same

conditions as particle tracking experiments in e-i. Black labeled markers indicate indenter position relative to the corresponding TPPS particle tracking images.

To examine the viability of our hypothesis we consider two scenarios, and use models to estimate the total excess energy that can be dissipated due to the periodic change in modulus. In the first model, shown schematically in Figure 5(a), we consider the difference in potential energy when a surface in contact with an indenter under normal load N, undergoes a change in modulus. (This represents the event in our experiments where the indenter slides from the stiff to the soft region.) Assuming that the velocity U is slow and the indenter comes to rest at its new position quickly, we can estimate the difference in potential energy of the two states using the Hertz contact theory. We assume this difference in potential energy is lost every time the indenter crosses a stiff-soft interface. In reality, contact is coupled with fluid flow and concomitant dissipation. However, the difference in potential energies provides an upper bound on the energy dissipation due to periodic variation in modulus. As such, the model is independent of the mechanism by which energy is dissipated; in our experiments that mechanism would evidently be through the radial in and out fluid flows.

If the system begins in the larger modulus state (LM) represented by the blue colored surface in Fig. 5a, and then changes to the smaller modulus state (SM) represented by the orange surface, the indenter (under normal load control) will move from an indentation depth δ_{LM} to δ_{SM}. The total potential energy of the system from this transition is presented in Figure 5(b), where the areas of the blue and orange regions represent the elastic (strain) energy stored for the larger modulus (U_{LM}) and smaller modulus (U_{SM}) states, respectively, while the grey area represents the change in potential energy of moving the external load from δ_{LM} to δ_{SM}. This transition will happen twice over one period, w, such that the effective excess contribution to friction force due to the modulus change, f_{MC}, is

$$f_{MC} = (N(\delta_{SM} - \delta_{LM}) - U_{LM} + U_{SM})\frac{2}{w} \quad . \qquad [6]$$

Based on Hertz contact theory[53], the strain energy is

$$U = (\tfrac{8}{15})(\tfrac{9}{16})^{5/6}(4G\sqrt{R})^{-2/3}N^{5/3} \qquad [7]$$

where R is the indenter radius and G is the shear modulus.[53] The values of δ_{LM} and δ_{SM} can be calculated using Hertz contact theory:

$$\delta = \frac{1}{R}(\frac{3NR}{16G})^{2/3} \quad . \qquad [8]$$

In order to compare it with experiments, we defined a measured excess frictional force for the TPPS, Δf_{TPPS}, as

$$\Delta f_{TPPS} = f_{TPPS} - 0.4 f_{Compliant} - 0.6 f_{Stiff} \qquad [9]$$

where, again, 0.4 and 0.6 represent the fraction of the TPPS surface area comprising each modulus phase. Values of Δf_{TPPS} are listed in Table 2 for the lower and upper limits of velocities tested (0.025 and 1 mm/s), along with the velocity independent value of f_{MC} for a given load and indenter

radius of 2mm. For all values except one (N=18.6mN, U=1mm/s) the f_{MC} is larger than Δf_{TPPS}. This establishes that there is sufficient energy change due the periodic change of modulus for its loss to account for essentially the entire frictional enhancement observed. That supports the hypothesis that the energy lost through the process of cyclic indentation of the surface as the modulus changes is a major mechanism behind the observed friction enhancement. Based on the observation of sudden rapid and periodic radial fluid flow in the contact region, it appears that this energy is being dissipated through the fluid.

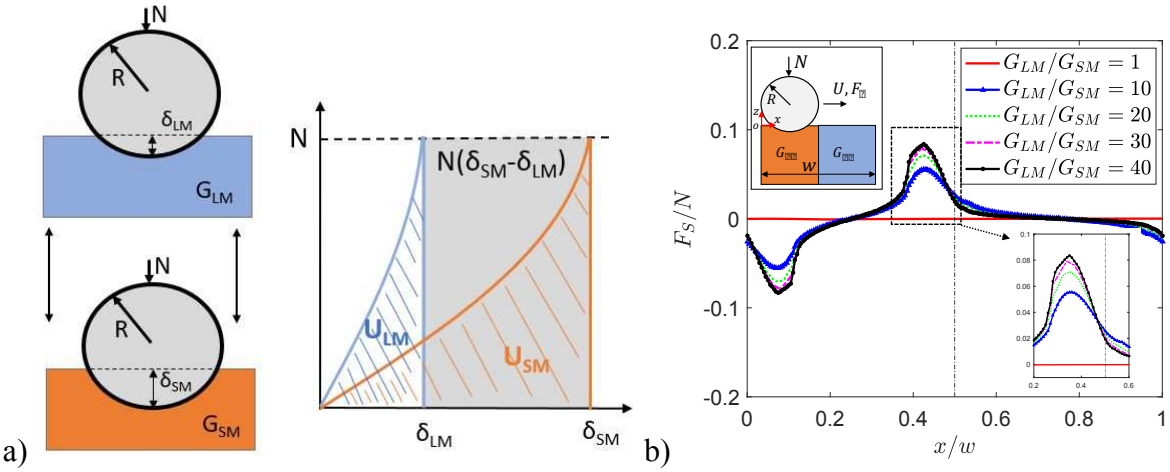

Figure 5. a) Schematic showing the two states (different modulus) between which the indenter cycles periodically. b) Finite element analysis of dry sliding on TPPS with R=2mm, w=2mm.

A second possible mechanism for the storage and irreversible release of energy comes from in-plane periodic deformation of the TPPS sample at the low and large modulus interface. FEM analysis of sliding a cylinder over a frictionless periodic surface was performed (details in SI). The frictional force resisting an indenter of radius and sample period, both of 2mm, due to elastic ploughing is shown in Figure 5(b). Because there is no intrinsic friction at the interface, the average friction force over a period is zero. However, if we assume that the energy stored in the system during increasing friction can be lost unstably during the decreasing friction part of the response, we can estimate the possible contribution from this mechanism to measured friction. We compute the energy by integrating F_s in the region where it is positive and increasing, up to the peak force, to estimate the how much excess energy could be dissipated by this mechanism. This happens twice a period such that

$$f_B = \frac{2R}{w}\int F_s dx \qquad [10]$$

Values of f_B for the loads used experimentally are also given in Table 2. It is immediately apparent that they are small compared to Δf_{TPPS} and f_{MC}, suggesting that while there may be some excess energy dissipated by elastic ploughing of the material during sliding, it is a small effect compared to measured friction and the contribution due to cyclic indentation. As it is proposed that energy is dissipated through the fluid, it appears this new form of elastic hysteresis does not rely on energy dissipation within the material itself. A second consequence of this fact is that under dry or boundary lubrication conditions, the intrinsic friction is likely to overwhelm this elastic hysteresis

effect, as we have indeed observed experimentally (see SI for dry results). A more complete model for this process of lubricated sliding over the TPPS sample requires a 3D, time dependent analysis of the unsteady EHL problem, which is the focus of ongoing work.

Table 2: Δf_{TPPS} for velocities of 0.025 and 1mm/s and calculated f_{MC} and f_B values for R=2mm indenter.

Load mN	Δf_{TPPS} U=0.025mm/s mN	Δf_{TPPS} U=1mm/s mN	f_{MC} mN	f_B mN
18.6	0.3	1.2	1.1	0.1
51.0	1.2	2.3	5.8	0.4
113.3	2.8	7.2	21.9	0.8
177.0	4.3	12.5	46.1	1.3
238.1	5.3	16.7	75.6	1.7

Conclusions

In this work we have found that sliding friction under EHL conditions can be significantly enhanced if the surface comprises a periodic pattern of soft and stiff regions. The primary mechanism for increased friction appears to be loss of potential energy during transitions of the contacting indenter between stiff and soft regions. We believe this to be a new form of elastic hysteresis that provides a novel mechanism by which to modulate lubricated friction, a problem of interest in a variety of technological and natural settings.

Acknowledgements This work was supported by the National Science Foundation, primarily by CMMI-1538002 and in part by CMMI-1854572. The authors would like to acknowledge useful discussion with Drs. Denis Mazuyer and Juliette Cayer-Barrioz.

References

1 Y. X. Wang, Y. P. Wu, W. J. Li and L. Q. Zhang, *Appl. Surf. Sci.*, 2011, **257**, 2058–2065.

2 Y. X. Wang, J. H. Ma, L. Q. Zhang and Y. P. Wu, *Polym. Test.*, 2011, **30**, 557–562.

3 A. (Alastair) Cameron, *Basic lubrication theory*, E. Horwood, 1976.

4 D. Dowson, G. R. Higginson, J. F. Archard and A. W. Crook, *Elasto-hydrodynamic lubrication*, Pergamon Press, 1977.

5 B. N. J. Persson, *Sliding Friction, Physical Principles and Applications*, Springer-Verlag, 2000.

6 E. H. Okrent, *ASLE Trans.*, 1961, **4**, 97–108.

7 S. T. Tzeng and E. Saibel, *ASLE Trans.*, 1967, **10**, 334–348.

8 B. L. S. Martz, *Proc. Inst. Mech. Eng.*, 1947, **16**, 1–9.

9 J. A. McGeehan, *SAE Trans.*, 1978, 2619–2638.

10 B. N. J. Persson and M. Scaraggi, *J. Phys. Condens. Matter*, 2009, **21**, 185002.

11 M. Scaraggi, G. Carbone, B. N. J. Persson and D. Dini, *Soft Matter*, 2011, **7**, 10395–10406.

12 M. Scaraggi, G. Carbone and D. Dini, *Soft Matter*, 2011, **7**, 10407.

13 J. M. Skotheim and L. Mahadevan, *Phys. Fluids*, 2005, **17**, 1–23.

14 B. Saintyves, T. Jules, T. Salez and L. Mahadevan, *Proc. Natl. Acad. Sci.*, 2016, **113**, 5847–5849.

15 E. Harrin, *Wear*, 1959, **2**, 492.

16 B. E. Sabey and G. N. Lupton, *Rubber Chem. Technol.*, 1964, **37**, 878–893.

17 K. A. Grosch and A. Schallamach, *Rubber Chem. Technol.*, 1976, **49**, 862–908.

18 Y. P. Wu, Y. Zhou, J. L. Li, H. D. Zhou, J. M. Chen and H. C. Zhao, *Wear*, 2016, **356**, 1–8.

19 M. Klüppel, Y. Bomal, A. Le Gal, L. Guy and G. Orange, *Wear*, 2007, **264**, 606–615.

20 H. K. Muller, *Fluid Sealing Technology: Principles and Applications*, Routledge, 1998.

21 F. Deleau, D. Mazuyer and A. Koenen, *Tribol. Int.*, 2009, **42**, 149–159.

22 A. Koenen and A. Sanon, *Tribol. Int.*, 2007, **40**, 1484–1491.

23 A. Borruto, L. Marrelli and F. Palma, *Tribol. Lett.*, 2005, **20**, 1–10.

24 Z. M. Jin and D. Dowson, *Proc. Inst. Mech. Eng. Part J J. Eng. Tribol.*, 2005, **219**, 367–380.

25 D. Dowson, *Solid Mech. its Appl.*, 2006, **134**, 297–308.

26 M. B. Jones, G. R. Fulford, C. P. Please, D. L. S. McElwain and M. J. Collins, *Bull. Math. Biol.*, 2008, **70**, 323–343.

27 W. G. Sawyer, A. C. Dunn, J. A. Tichy and J. M. Uruen, *Tribol. Int.*, 2013, **63**, 45–50.

28 M. J. Adams, B. J. Briscoe and S. A. Johnson, *Tribol. Lett.*, 2007, **26**, 239–253.

29 J. F. Prinz, R. A. de Wijk and L. Huntjens, *Food Hydrocoll.*, 2007, **21**, 402–408.

30 M. E. Malone, I. A. M. Appelqvist and I. T. Norton, *Food Hydrocoll.*, 2003, **17**, 763–773.

31 Y. Wang, C. Dhong and J. Frechette, *Phys. Rev. Lett.*, 2015, **115**, 248302.

32 Y. Wang, M. R. Tan and J. Frechette, *Soft Matter*, 2017, **13**, 6718–6729.

33 F. Kaveh, J. Ally, M. Kappl and H. J. Butt, *Langmuir*, 2014, **30**, 11619–11624.

34 S. Leroy, A. Steinberger, C. Cottin-Bizonne, F. Restagno, L. Léger and I. Charlaix, *Phys. Rev. Lett.*, 2012, **108**, 264501.

35 J. De Vicente, J. R. Stokes and H. A. Spikes, *Tribol. Lett.*, 2005, **20**, 273–286.

36 J. H. H. Bongaerts, K. Fourtouni and J. R. Stokes, *Tribol. Int.*, 2007, **40**, 1531–1542.

37 C. Myant, H. A. Spikes and J. R. Stokes, *Tribol. Int.*, 2010, **43**, 55–63.

38 M. Scaraggi, G. Carbone and D. Dini, *Tribol. Lett.*, 2011, **43**, 169–174.

39 J. M. Kim, F. Wolf and S. K. Baier, *Tribol. Int.*, 2015, **89**, 46–53.

40 S. Stupkiewicz, J. Lengiewicz, P. Sadowski and S. Kucharski, *Tribol. Int.*, 2016, **93**, 511–522.

41 N. Selway, V. Chan and J. R. Stokes, *Soft Matter*, 2017, **13**, 1702–1715.

42 P. Sadowski and S. Stupkiewicz, *Tribol. Int.*, 2019, **129**, 246–256.

43 G. Tan, D. Wang, S. Liu, H. Wang and S. Zhang, *Sci. China Technol. Sci.*, 2013, **56**, 3024–3032.

44 A. Jagota and C. Y. Hui, *Mater. Sci. Eng. R Reports*, 2011, **72**, 253–292.

45 S. Kim and M. Sitti, *Appl. Phys. Lett.*, 2006, **89**, 261911.

46 Y. Bai, C.-Y. Hui, B. Levrard and A. Jagota, *Langmuir*, 2015, **31**, 7581–7589.

47 Z. He, C. Y. Hui, B. Levrard, Y. Bai and A. Jagota, *Sci. Rep.*, 2016, **6**, 26867.

48 N. Moyle, Z. He, H. Wu, C. Y. Hui and A. Jagota, *Langmuir*, 2018, **34**, 3827–3837.

49 D. Gropper, L. Wang and T. J. Harvey, *Tribol. Int.*, 2016, **94**, 509–529.

50 L. Shen, N. J. Glassmaker, A. Jagota and C.-Y. Hui, *Soft Matter*, 2008, **4**, 618.

51 G. G. Genchi, G. Ciofani, I. Liakos, L. Ricotti, L. Ceseracciu, A. Athanassiou, B. Mazzolai, A. Menciassi and V. Mattoli, *Colloids Surfaces B Biointerfaces*, 2013, **105**, 144–151.

52 J. Y. Tinevez, N. Perry, J. Schindelin, G. M. Hoopes, G. D. Reynolds, E. Laplantine, S. Y. Bednarek, S. L. Shorte and K. W. Eliceiri, *Methods*, 2017, **115**, 80–90.

53 K. L. Johnson, *Contact Mechanics*, Cambridge University Press, 1985.